

# Overcoming Data Scarcity in Biomedical Imaging with a Foundational Multi-Task Model

Raphael Schäfer<sup>1</sup>, Till Nicke<sup>1</sup>, Henning Höfener<sup>1</sup>, Annkristin Lange<sup>1</sup>, Dorit Merhof<sup>1,3</sup>, Friedrich Feuerhake<sup>4,5</sup>, Volkmar Schulz<sup>1,2</sup>, Johannes Lotz<sup>1†</sup> and Fabian Kiessling<sup>1,2†</sup>

<sup>1</sup>Fraunhofer Institute for Digital Medicine MEVIS.

<sup>2</sup>Institute for Experimental Molecular Imaging, RWTH Aachen University.

<sup>3</sup>Institute of Image Analysis and Computer Vision, Faculty of Informatics and Data Science, University of Regensburg.

<sup>4</sup>Institute for Pathology, Hannover Medical School.

<sup>5</sup>Institute for Neuropathology, University Clinic Freiburg.

†JL and FK contributed equally to this work.

## Abstract

Foundational models, pretrained on a large scale, have demonstrated substantial success across non-medical domains. However, training these models typically requires large, comprehensive datasets, which contrasts with the smaller and more heterogeneous datasets common in biomedical imaging. Here, we propose a multi-task learning strategy that decouples the number of training tasks from memory requirements. We trained a Universal bioMedical PreTrained model (UMedPT) on a multi-task database including tomographic, microscopic, and X-ray images, with various labelling strategies such as classification, segmentation, and object detection. The UMedPT foundational model outperformed ImageNet pretraining and the previous state-of-the-art models. For tasks related to the pretraining database, it maintained its performance with only 1% of the original training data and without fine-tuning. For out-of-domain tasks it required not more than 50% of the original training data. In an external independent validation imaging features extracted using UMedPT proved to be a new standard for cross-center transferability.

**Keywords:** Foundation models, Multi-task learning, gradient-accumulation, generalization

## Main

Deep learning has started to revolutionize biomedical image analysis, owing to its ability to learn and extract useful image representations. A widely-adopted approach for enabling deep learning in biomedical image analysis involves pretraining models on extensive natural image datasets, such as ImageNet-1K [1], and subsequently either fine-tuning them or utilizing pre-trained features directly for specific target tasks [2–4]. Fine-tuning leverages the pretrained model’s weights as initial foundation, enabling accelerated training and enhanced performance even in situations with limited data. Alternatively, such foundational models can be kept frozen, with their features directly applied to biomedical downstream tasks. Despite requiring more computation time and data amounts, fine-tuning has firmly established itself as standard practice across a diverse range of downstream computer vision tasks, encompassing object detection and semantic segmentation, among others [5, 6].

Driven by the recent trend of increasingly large pretrainings, the need for foundational models in biomedical imaging has become clear [7, 8]. However, effective pretraining of deep neural networks requires large amounts of annotated training data, which are often scarce in biomedical imaging [9]. While many public small and medium-sized datasets exist in the biomedical domain, there is no single pretraining dataset comparable to ImageNet.

Several methods have been proposed to address the data scarcity problem when pretraining deep networks for biomedical image analysis. One approach is to use self-supervised learning, which learns visual representations from unlabeled data by solving pretext tasks. However, clear performance gaps exist between self-supervised and label-supervised pretraining methods [10].

Another approach is to use domain-specific supervised pretraining. For example, Zhou et al. [10] used a large text-labeled chest X-ray dataset to train universal representations for chest X-rays. They evaluated their approach on unseen datasets and found that their chest X-ray encoder outperforms ImageNet pretraining by up to 10% accuracy when applied to other chest X-ray analysis tasks. Nonetheless, supervised pretraining can only be applied to domains where large amounts of training data are available, such as radiographs.

Mei et al. [4] proposed to combine multiple medical classification datasets into one larger dataset and use it for pretraining deep networks for radiology tasks. They presented target tasks where this approach can achieve better results than ImageNet pretraining. However, this approach has limitations: it relies solely on classification labels, which may not capture all relevant information in medical images, and it requires the network to predict all classes in the combined dataset, even if they are unrelated or not meaningful for a given case.

Multi-task learning (MTL) promises to provide a solution to data scarcity in biomedical image analysis by enabling simultaneous training of a single model that generalizes well across multiple tasks [11]. It takes advantage of the many small- and medium-sized datasets in biomedical imaging, efficiently

utilizing different label types and data sources to pretrain image representations which are applicable to all tasks, enabling deep learning for domains with sparse data. MTL has been applied to biomedical image analysis in various ways, such as training on multiple small- and medium-sized datasets from distinct tasks, specifically limited to classification [12] or segmentation [13]. Additionally, MTL has been used with multiple label types for individual images, demonstrating that sharing features across label types enhances task performance [14].

To combine multiple datasets with different label types for large-scale pretraining, we introduce a novel multi-task training strategy specifically designed to address the data scarcity problem in biomedical imaging by learning versatile representations across diverse biomedical modalities, diseases, and label types. To cope with the memory constraints commonly encountered in large-scale multi-task learning, our approach employed a gradient accumulation-based training loop whose scaling is almost unconstrained with respect to the number of training tasks.

Figure 1 presents the architecture of our neural network which consisted of shared blocks, such as the encoder, a segmentation decoder, and a localization decoder, along with task-specific heads. The shared blocks were trained for application to all pretraining tasks, facilitating the extraction of universal features, while the task-specific heads handled label-specific loss calculation and predictions. Our tasks included three supervised label types: object detection, segmentation, and classification. Classification tasks, for instance, can model binary biomarkers, segmentation tasks can extract spatial information, and object detection tasks can be used, for example, to train biomarkers based on cell quantities.

Using this architecture and training strategy, we developed, to our knowledge, the first fully supervised foundational model for biomedical imaging named UMedPT, using 17 tasks based on 15 datasets and their original annotations. Each task consisted of training and test sets with its label type, e.g., classification, segmentation, or object detection. A study overview is presented in Figure 1.

## 4 UMedPT - Foundational Biomedical Pretraining

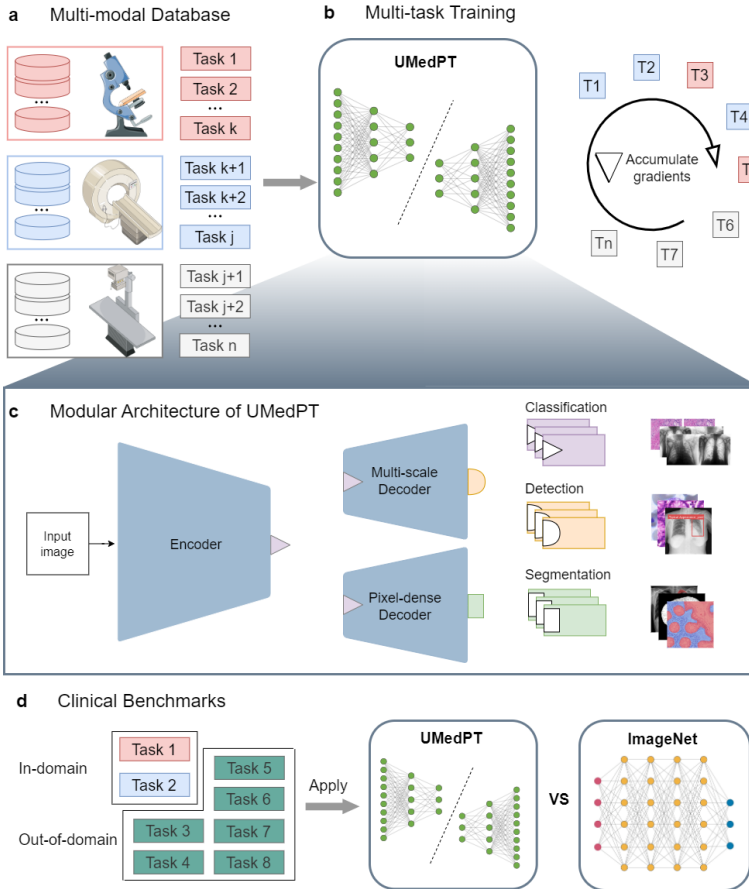


**Fig. 1 Study Overview.** Illustration of the organization of the study and the multitask learning approach: **a** Heterogeneous data sources from histology (red), tomographic imaging (blue), and X-ray (gray) formed the generalized training database. **b** The pretraining process trained generally applicable neural network components (shared blocks). A novel training loop based on gradient accumulation, detailed in Algorithm 1, allowed for the joint training incorporating all pretraining tasks at each optimization step despite different label types. **c** Depending on the label type of the current task being processed, our modular architecture was assembled from a set of three shared blocks. More information about each shared block can be found in Figure 4. **d** The applicability of the pretrained neural components to medical imaging was evaluated using a diverse benchmark consisting of several clinically relevant small datasets categorized as in-domain or out-of-domain. The performance of UMedPT was compared with that of ImageNet pretraining.

UMedPT consistently matched or outperformed the pretrained ImageNet network in in- and out-of-domain tasks, while maintaining strong performance with substantially less training data in both direct application of image representations (frozen) and fine-tuning settings. Furthermore, we compared our model with external reference results and demonstrated the robustness of UMedPT through external validation.

By providing the training framework and model as open-source software, we facilitate the training and implementation of data-efficient biomedical imaging models. Serving as a basis for future advancements in data-scarce domains, UMedPT opens perspectives to extend the application of deep learning in medical fields where collecting large cohorts is particularly challenging, such as rare diseases and pediatric imaging.

## Results

We designed two benchmarks: the “in-domain benchmark” to assess the applicability of UMedPT to problems closely related to its training database and the “out-of-domain benchmark” to evaluate its performance in unfamiliar domains. Additionally, we compared our findings with previously published results from the same datasets being considered the state of the art.

Furthermore, we assessed UMedPT’s performance in data-scarce scenarios by training it with varying amounts of original training data, ranging from 1% to 100%, and report the average results gathered from five repeated runs for each experimental setup. All networks were trained with a frozen encoder and subsequently in a fine-tuning setting with the same training scheme and hyperparameters.

Ablation studies are included in Extended Data Tables 1, 2 and 3. First UMedPT-fixed, which consistently used an image size of (224, 224), and UMedPT-A, which retains the same image dimensions but replaces static layernorms with trainable (affine) layernorms. In our evaluations across various tasks, UMedPT outperformed ImageNet by an average of 8.5% and surpassed UMedPT-fixed by 2.97%. Compared with UMedPT-fixed, UMedPT-A showed an average performance gain of 0.37%.

### **For in-domain tasks, UMedPT matches the baseline performance with 1% of the data without fine-tuning**

We compared UMedPT to results obtained with weights pretrained on ImageNet. In both tasks, UMedPT was able to match the best performance of the ImageNet baseline over all configurations using only 1% of the original training data. Notably, our model achieved higher performance with a frozen encoder compared to our model with fine-tuning, as shown in Figure 2. Below, we outline key findings in two in-domain tasks.

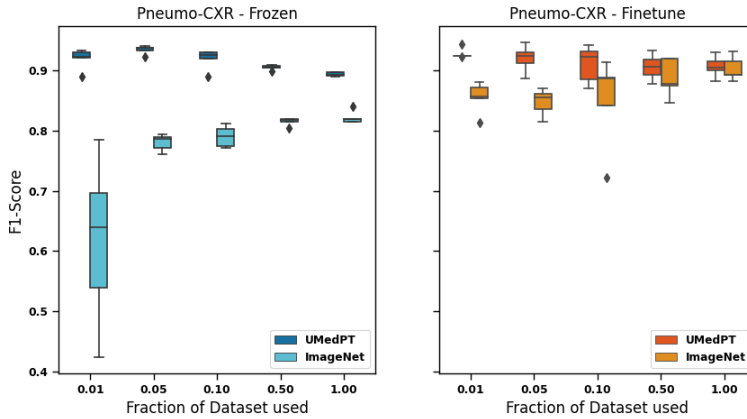
#### ***CRC tissue classification (CRC-WSI):***

In CRC-WSI, we classified colorectal cancer (CRC) tissue from microscopic whole slide images (WSI) into nine different classes, including adipose tissue, normal colon mucosa, and colorectal adenocarcinoma epithelium [15].

ImageNet achieved an average F1-score of 95.2% in predicting the nine different tissue classes on the unseen test set using all of the training data and fine-tuning. UMedPT achieved a comparable performance with 1% training data and a frozen encoder (95.4% F1-score, see Figure 2).

6 *UMedPT - Foundational Biomedical Pretraining*

a



b

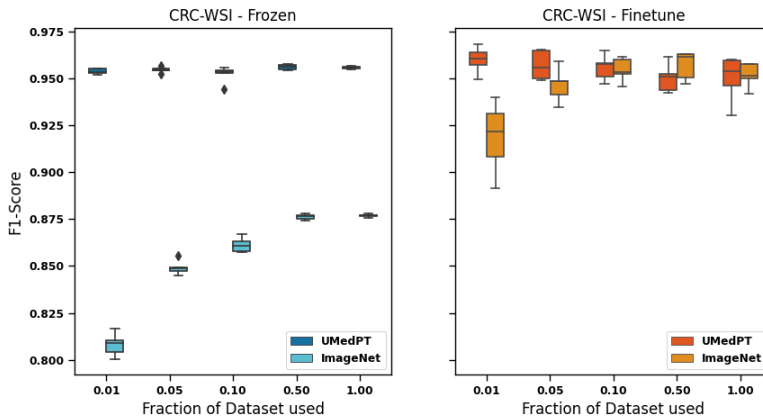


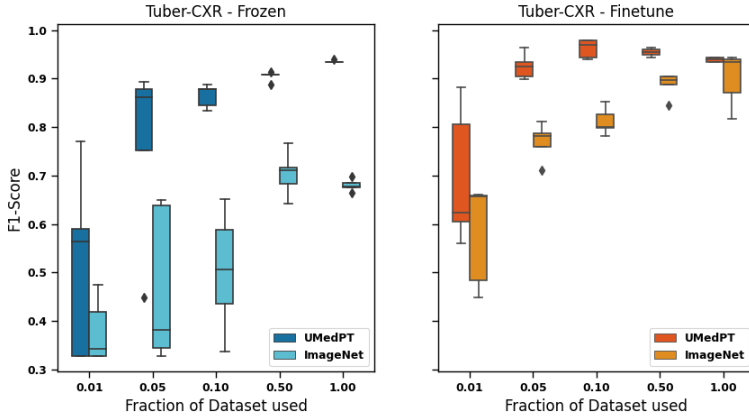
**Fig. 2 Results for in-domain tasks.** **a** In diagnosing tuberculosis (Tuber-CXR), UMedPT matched the full fine-tuned performance of ImageNet, even with a frozen encoder and a reduced dataset size (50%). **b** For BC-Bach-WSI, fine-tuning was essential for high performance. When the encoder was frozen, half the training data was required to match the result obtained with ImageNet in a similar setting.

When the training dataset size was increased to 50% and 100% and the models were fine-tuned, the results converged to approximately the same F1-score across all methods (Extended Data Table 1). Surprisingly, for UMedPT, increasing the training data beyond 1% did not enhance the model’s performance and sometimes tended to degrade it. Notably, it did not matter which 1% were picked as the final performance had a low variance.

### *Pneumonia in pediatric cohort (Pneumo-CXR):*

Pneumo-CXR focused on diagnosing pediatric pneumonia [16]. Here, UMedPT outperformed ImageNet across all dataset sizes. The best performance of

a



b

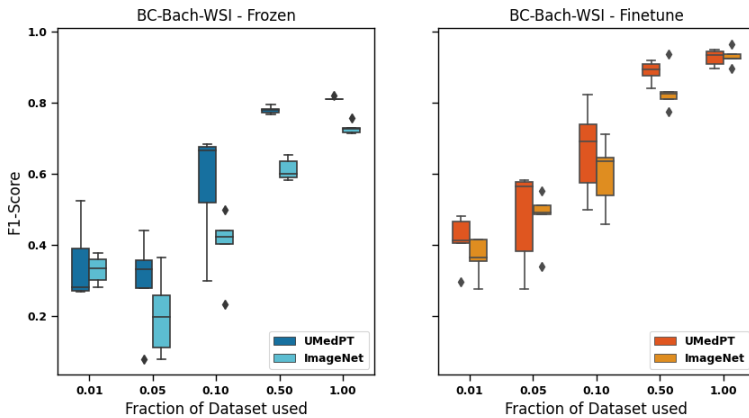


**Fig. 3 Results for out-of-domain tasks.** **a** For tuberculosis diagnosis (Tuber-CXR), UMedPT enables matching the full ImageNet performance even with frozen encoder and a reduced amount of data (50%). **b** In BC-Bach-WSI, fine-tuning was necessary for a high performance. In the frozen setting, half of the training data was required to match the ImageNet frozen result.

UMedPT was achieved using 5% of the data ( $\approx 250$  images) and frozen features, resulting in an F1-score of 93.5%. The best ImageNet performance (90.3% F1-score, 100% of the data) was matched with the smallest split (1% of the data,  $\approx 50$  images, see Extended Data Table 1).

### For out-of-domain tasks, UMedPT maintains ImageNet performance despite reduction in training data

In the out-of-domain benchmark, UMedPT compensated a data reduction of 50% or more across all datasets in the benchmark when the encoder was frozen,

as detailed in Extended Data Table 2. With fine-tuning, ImageNet’s performance consistently improved if more data were used. Here, for two out of five datasets, UMedPT was able to match the performance of ImageNet using only 50% or less of the data, even when fine-tuning was applied (see Figure 3 and Extended Data Table 3). Below, we highlight key findings in the out-of-domain tasks:

***Tuberculosis diagnosis in CXR (Tuber-CXR):***

In the task of diagnosing tuberculosis from chest X-ray (CXR) [17], UMedPT delivered the highest average result. This was achieved by fine-tuning the model and using just 10% of the data, resulting in an F1-score of 96.3%. Adding more training data did not further improve the score for our model (Figure 3). To match the overall best average result of ImageNet, UMedPT required 5% of the data with fine-tuning and 50% of the data with a frozen encoder.

***CNS neoplasia diagnosis in MRI (CNS-MRI):***

We used the CNS-MRI [18] dataset to train our system to diagnose CNS neoplasms from MRI scans. ImageNet, with frozen features, achieved an F1-score of 89.0%. UMedPT was able to match this score using 5% of the training data. With the full training set and fine-tuning, UMedPT achieved the top F1-score of 99.3%.

***Breast cancer classification in WSI (BC-Bach-WSI):***

The BC-Bach-WSI dataset was used for breast cancer classification in whole slide images. Using the frozen encoder, ImageNet achieved an F1-score of 72.9%. UMedPT obtained this score with 50% of the data, resulting in an F1-score of 78.0%. Here, the best results were achieved using fine-tuning.

***Breast cancer classification in microscopic images (BC-BHis-MIC):***

The BC-BHis-MIC dataset was used for breast tumor classification into benign and malignant in microscopic (MIC) images. The best mean ImageNet result was achieved with 100% of the data and fine-tuning, resulting in an F1-score of 98.4%. UMedPT also achieved an F1-score of 98.4%. When using a frozen encoder, ImageNet achieved an F1-score of 82.3%. UMedPT was able to match this score using 50% of the data.

***Organ segmentation in MRI (OrganSeg-MRI):***

The OrganSeg-MRI dataset [19] was used for organ segmentation in MRI scans. Training with the frozen encoder did not yield satisfactory results, neither for ImageNet nor for UMedPT. The best average baseline result was observed when using 100% of the data and fine-tuning, resulting in a mean Intersection over Union (mIoU) of 0.859. Even in this setting, UMedPT outperformed ImageNet, achieving an mIoU of 0.881. UMedPT needed 50% of the data to match the best ImageNet result.

## Comparison of UMedPT with external reference results

Next, we compared the performance of UMedPT to outcomes reported in the literature. When using the frozen encoder configuration, UMedPT surpassed the external reference results in four out of six tasks. Notably, the two tasks where UMedPT underperformed were out-of-domain (breast cancer classification BC-Bach-WSI and CNS neoplasia diagnosis CNS-MRI).

With fine-tuning, UMedPT exceeded the external reference results across all tasks (see Table 1).

A comparison for the OrganSeg-MRI task could not be performed, because no results specific to the MRI-only subtask of the challenge were reported. The reference results are further detailed in the supplement, Section S1.

For the two in-domain target tasks, 1% of the original training data were enough to reach the external reference results. For out-of-domain tasks UMedPT required  $\leq 50\%$  of the original training data to match the state-of-the-art performance when fine-tuning is used. With frozen features, in three out of four tasks UMedPT required either 100% of the data or did not match the state of the art.

**Table 1** Amount of data required by UMedPT to match state-of-the-art performance on classification tasks from different imaging domains. Datasets marked with an asterisk (\*) were compared across different test splits.

Task	Reference results	UMedPT	
		Frozen	Fine-Tuning
CRC-WSI	> 94% accuracy [15]	1%	1%
Pneumo-CXR	92.8% accuracy [16]	5%	1%
Tuber-CXR*	82% accuracy [20]	10%	5%
Tuber-CXR*	98.0% AUC [10]	50%	10%
CNS-MRI*	> 96% accuracy	-	50%
BC-Bach-WSI*	87% accuracy [21]	-	50%
BC-BHis-MIC*	88% F1-score [22]	100%	10%

## UMedPT provides robust image representations across clinical centers

*Due to an embargo this section will be updated after 01.01.24*

## Discussion

Using a novel multi-task training strategy, UMedPT fuses knowledge from multiple sources to compute robust image representations across diverse biomedical modalities, diseases, and label types. We demonstrate that this knowledge can be effectively transferred to unseen target tasks. Similarly, previous studies reported that pretraining on a large dataset [10] or multi-task pretraining [12] can improve models' performance on small, unseen datasets. In the field of medicine, this is, for example, especially important for rare and

pediatric diseases, where the quantity of available images is often too small to effectively train deep neural networks. However, the performance advantage of UMedPT in in-domain tasks compared to out-of-domain tasks indicates that it is not entirely universal for all biomedical imaging applications yet, necessitating a broader scale of training. The extent to which such pretraining should be scaled remains an open question. In natural language processing, larger models have demonstrated improvements with scaling, with some studies using up to 540 billion parameters [23]. However, even non-biomedical foundational vision models, which are not limited by data scarcity, are 10 to 1000 times smaller than their natural language counterparts [24, 25]. This suggests that large vision models may not require an excessive number of parameters. Nevertheless, larger models typically require larger datasets, and our approach of combining labeled datasets into a single training could facilitate scaling of foundational vision models.

Alternatively, self-supervised pretraining can be applied. However, recent literature has proposed that label-supervised pretraining for imaging typically outperforms self-supervised pretraining empirically [10, 26] and theoretically [27]. Nonetheless, it still offers value in regularizing models and might help in reducing the volume of labelled data necessary. Our approach can be extended to include an arbitrary number of self-supervised tasks into the pretraining, which may further enhance the generalizability of UMedPT, especially in domains where abundant data are available but labelling is difficult or costly.

Training AI models from scratch can be computationally intensive. Here, foundational models such as UMedPT in a frozen configuration may enable efficient feature extraction without additional training. Frozen features from pretrained networks solved in-domain classification tasks in pathology [12] and radiology [28, 29]. For natural images, the authors of CLIP [24] mentioned strong performance when directly reusing their frozen model for unseen tasks [24]. However, the performance declined when frozen models were used for out-of-domain evaluations. Our in-domain benchmark results are consistent with these findings, suggesting that frozen features should be the primary consideration for in-domain tasks. Moreover, we demonstrate that a single network can effectively extract features across multiple domains, extending the applicability of frozen features within the in-domain context.

We show that for out-of-domain tasks, fine-tuning can outperform the frozen configuration if there are enough data or significant differences between the target task data distribution and the pretraining distributions. Other multi-task studies [12] have observed that fine-tuning multi-task models or pretrained ImageNet models yield comparable performance. However, even with fine-tuning, ImageNet did not outperform UMedPT in any medical applications evaluated. In fact, UMedPT showed advantages in the full data scenario with fine-tuning in two out-of-domain tasks. This could potentially be due to either the larger scale of UMedPT's training, which resulted in a well-generalizing base for fine-tuning, or the possibility that these two out-of-domain datasets were not sufficiently large at full size, making them ideal use cases for UMedPT.

Differences in imaging modalities, scanners, annotations, or patient populations can make models fail when applied to data of different clinical centers [30]. Foundational models should be robust to multi-center variances, thereby improving their ability to generalize. *Due to an embargo this section will be updated after 01.01.24*

Medical images vary in size, challenging deep learning methods that typically require uniform sizes. Homogeneous downsampling, however, resulted in reduced performance when comparing UMedPT and UMedPT-fixed, which is consistent with previous findings [13]. For tasks that benefit from a large image size, our training method allows flexibility in choosing the optimal image size for each task, thus avoiding the problem of pre-defining it.

In conclusion, we demonstrated that the knowledge transfer capabilities of UMedPT reduce the amount of data and time needed to train models for unseen tasks. In addition, UMedPT can effectively manage domain shifts, thereby improving diagnostic performance in unfamiliar domains, such as pediatric cohorts or cohorts of unknown ethnicity. Our results show that direct application of UMedPT in a frozen setting can save time and computational resources while maintaining robustness across research centers and achieving state-of-the-art performance. Even with large data and fine-tuning, we found no cases where ImageNet performed better than UMedPT. Thus, we hypothesize that UMedPT is a valuable foundational model for biomedical imaging, especially when data are scarce. Both the pretrained model and the multi-task training framework are available on Github (<https://...url-will-be-added-in-final-version>).

## Methods

In deep learning, training of models is performed by optimizing an objective function (loss function) that measures the difference between ground-truth labels and the result of the current models' iteration. The gradient of the loss function determines the extent of adjustments needed for each model parameter.

In the presented multi-task learning framework, the overall loss of the model was defined as the sum of the losses of all tasks that were evaluated simultaneously.

Every label type required the definition of a task-specific architecture component and an objective function computing its loss. For UMedPT, we combined these different components into a single model to solve many pretraining tasks simultaneously. These pretraining tasks integrated a large variety of the publicly available biomedical image data, including their annotations, into a single foundational training. This training led to a shared model compatible to all of the pretraining tasks.

We addressed challenges such as memory constraints, varying input sizes, and label types to integrate a diverse set of small and medium-sized datasets for training UMedPT. The model's design accommodated a variety of task

types, including classification and dense-prediction tasks like segmentation, and allowed each task to operate using its optimal patch size and resolution, respectively.

## Multi-task training strategy

A limiting factor in scaling currently established multi-task learning approaches is the increasing memory demand that is proportional to the number of tasks. This memory need is caused by processing all tasks in parallel during a single network pass. To address this challenge, we developed a novel training strategy for UMedPT that mostly decouples the number of training tasks from the memory requirements.

Our strategy achieved this by establishing an independent architecture, or 'computational graph', for each task. This graph is dynamically constructed and stored only during the active computation stage of each task. To combine the individual graphs, we implement gradient accumulation (GA) before the optimization step as described in Algorithm 1. GA allowed us to establish a training scheme wherein a single update step can consist of heterogeneous tasks in any order.

We ensure that the model's weights and gradients are stored only once, rather than duplicating them for each task. Additionally, only the activations for one task are kept in memory at a time. They are discarded after each task's backward pass, rather than stored for all tasks simultaneously. Therefore, the only memory requirements that increase with the number of tasks are related to the gradients of each task's head. As the shared section of the model represents the majority of the total model size, this approach allows for multi-task learning across many tasks, even on hardware with limited computational power.

Unlike traditional training schemes which merge multiple tasks in a batch of samples, GA enables flexible task scheduling. Each optimization step can therefore consist of multiple tasks and even multiple instances of the same task, enhancing the versatility of the proposed training approach.

When training a model on many tasks, the size of the respective dataset should not implicitly influence the task's weight in the overall model. To accommodate datasets of different sizes, we implemented an "infinite task sampler", which yielded one training batch of each task for every optimization step. Once all data points of a task were used, the task sampler independently restarted the data loading for this task. No information on the dataset's length was needed beforehand, which allowed each epoch to have a different length depending on data augmentation. When training a multi-task model with GA, the model parameters were updated according to the sum of the model's gradients. Because summation is commutative, the order of tasks within an optimization step does not affect the outcome.

Classification, segmentation, and detection tasks have different loss functions with greatly varying magnitudes. This can lead to a situation where the loss of one task dominates the combined loss, resulting in insufficient training

of other tasks. To counteract this, we normalized the respective loss functions for each task type such that the expected value for random inputs for re-initialized weights was close to one.

We uniformly used the AdamW optimizer [31] for all parameters. Following the training settings of [32] for ImageNet-1K training, we used a learning rate of 0.001 and a weight decay of 0.05 for all transformer-based models.

---

**Algorithm 1** The training loop processed tasks and their associated batches in the order given by the task sampler. For each step, a gradient was computed by evaluating the objective function of one task with respect to one of its batches. These gradients were accumulated until the task sampler initiated an optimization step. At this point, model parameters were updated considering all tasks since the last update, utilizing the accumulated gradient. After this, the gradient buffer was cleared for the next cycle.

---

```

1: procedure TRAIN(stepsPerEpoch, sharedblocks, tasksampler, optim)
2:   prepareSharedBlocks()           ▷ norm & task-specific modules
3:   optim.clearGradients()
4:   for step ← 0 to stepsPerEpoch do
5:     (batch, task) ← tasksampler.next()
6:     loss ← task.computeLoss(batch, sharedblocks)
7:     loss.backward()                 ▷ Accumulate gradients
8:     if isUpdateStep(step) then   ▷ E.g. after processing each task
9:       optim.updateParams()
10:      optim.clearGradients()
11:    end if
12:  end for
13: end procedure

```

---

## Architecture

Our tasks vary in their label types, each requiring problem-specific architectures. Therefore, we used a fixed-size embedding for classification tasks, designed to encapsulate features that are useful across all tasks. For segmentation tasks, we implemented a U-Net-like encoder-decoder scheme to learn multi-scale features. Additionally, object detection using FCOS [33] required features produced by a feature pyramid network [34].

To avoid wasting resources as not all features are required for every task, we created a modular architecture. We hypothesized that parameters should be largely shared across tasks. To address this, we placed most parameters into a shared encoder. To compute the necessary types of features, we then developed a pixel-dense decoder and a multi-scale decoder.

Our architecture supported encoders with configurable settings for image embedding dimensionality, stride (modulating the spatial range of feature pyramid levels), and feature pyramid depths. Given these settings are common

in computer vision, our framework was able to integrate open-source encoder architectures. For segmentation tasks, we used a pixel-dense decoder that upsampled the feature pyramids in a U-Net style to generate pixel-features. For object detection, a multi-scale decoder was used to create feature maps from every pyramid level.

For the classification tasks, we directly used the image embedding from the encoder. This was computed using global average pooling from the lowest level of the feature pyramid, allowing us to handle variable input sizes. This approach is consistent with the ImageNet baseline. Segmentation tasks employed the shared pixel-dense decoder, while object detection tasks processed the encoder’s output via a shared feature pyramid network. The output for each label type was computed using a single linear layer, or a single convolutional layer for dense prediction tasks.

In general, our proposed training loop can be used with any neural network, and UMedPT’s decoders are compatible with any encoder that can generate multi-scale feature maps. We chose Swin Transformers as the encoder for UMedPT [32]. They introduced a shifted windowing scheme that improved the efficiency of vision transformers with respect to image input size.

Regardless of the chosen architecture, normalization has been shown to be essential for accelerating the training process [35, 36]. Batch normalization [35] is a widely used normalization technique. However, in our experiments, batch normalization led to poor performance (results not shown). One assumption when using batch normalization is that all input batches follow a common distribution which can be parameterized by a common statistical distribution. When combining different tasks and datasets, this assumption no longer holds.

While we observed that normalization layers enhanced training speed, they negatively impacted generalization within our training strategy. We found that the issue only arose when normalization statistics were computed across different tasks. To address this problem, we recursively replaced the original normalization layers in all shared blocks with layer normalization [36], which by design do not require inter-task computation. This modification enabled the model to concurrently generalize across multiple training tasks.

We empirically analysed the effect of using layernorms with affine parameters in an adaptation UMedPT-A. UMedPT-A was trained under the same setting as UMedPT-fixed.

## Data loading from diverse sources

To evaluate the ability of the model to learn multi-modal representations, we integrated a diverse range of biomedical imaging data types — including microscopic pyramid gigapixel 2D images, standard 2D images (both grayscale and color), and 3D tomographic images — into a single network. Each data type requires unique pre-processing and domain-specific augmentations for a universally applicable deep learning solution. To accommodate these different

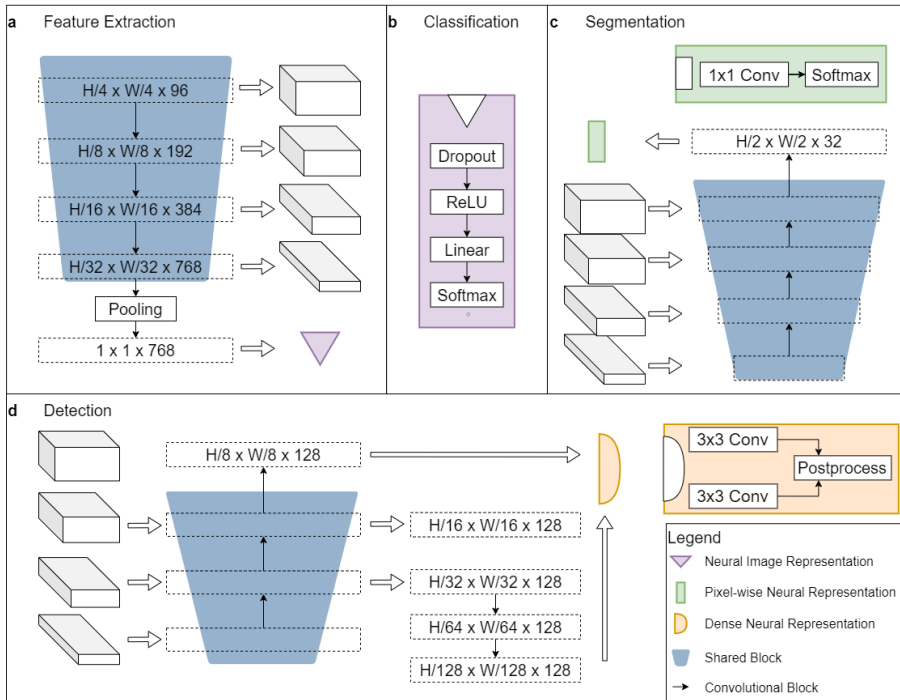


**Fig. 4 UMedPT’s architecture.** **a** Features are extracted from an image of size  $H \times W$  through a shared encoder. **b** Classification heads take the neural image representation of an image and apply a single linear layer. **c** A shared pixel-wise decoder processes the multi-scale feature maps and returns an embedding per pixel. Segmentation heads employing the popular U-Net spatial decoding strategy for handling segmentation features generate the prediction. **d** The multi-scale decoder uses the feature maps and transforms them into features for box-regression and box-classification. The FCOS-based detection head generates the final prediction.

data types, the encoder of UMedPT used a standardized 2D image input format. This required the conversion of each data type into a two-dimensional format, as illustrated in Figure 5.

To ensure compatibility between different data types, we normalized all pixel intensities to a range between 0 and 1. For images with values ranging from 0 to 255, we divide them by 255. For 3D images, we normalize the maximum in the volume to 1 and the minimum to 0 for CT, and for MRI the intensity quantiles (2.5%, 97.5%) were used.

Smaller two-dimensional images from modalities like X-ray imaging, were resized to an edgelenhth of around 512 pixels. For larger images from histopathology, we extracted patches of similar size. Three-dimensional volumes were cut into slices to adapt them to the 2D format with task-specific patch sizes ranging from 224 to 512. Images did not need to be square for our training strategy.

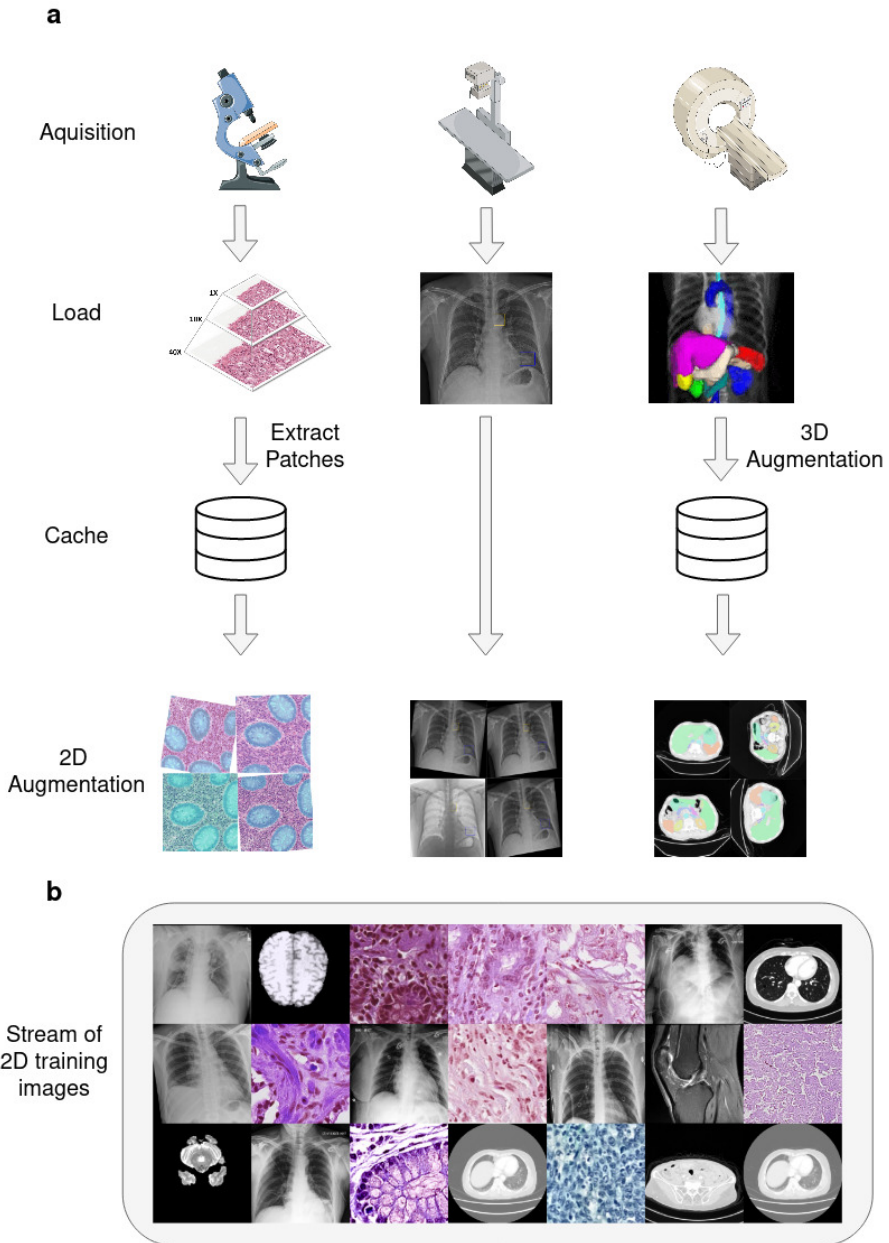


**Fig. 5 Data pre-processing.** **a** We have categorized all of our tasks into one of three common formats: 2D images, 3D tomographic images, and gigapixel images. For each format, we developed a data loading strategy that transforms the data into the required 2D format. Additionally, for each domain, we implemented a standard augmentation strategy to be applied to the corresponding 2D images. **b** Our preprocessing results in a diverse stream of data including samples from all tasks.

We used a caching component to load whole slide images and 3D volumes. This method eliminated the need for pre-extraction of images, thereby enhancing data diversity. 3D augmentations were applied during every initial loading, while patch augmentations occurred when a patch was retrieved from the cache.

### ***Pretraining Tasks***

We selected 15 publicly available datasets for pretraining and extracted 17 tasks from them. We prioritized datasets that demonstrated acceptable performance in a single task setting. We defined acceptable performance as either aligning with the metrics reported by the dataset creators, when feasible, or passing a plausibility check conducted by a medical expert. Following these selection criteria, we included the following datasets in our study:

- Amos22-CT organ segmentation in CT [19]
- Conic-WSI cell detection [37]
- PICAL-MRI prostate cancer classification [38]
- Panda-WSI prostate tissue semantic segmentation [39]
- Panda-WSI prostate tissue classification [39]
- VinBigData-CXR Thorax pathology pathology detection [40]
- Crag-WSI Colorectal tissue semantic segmentation [41]
- Brats2020-MRI brain semantic segmentation [42]
- CRC-WSI colorectal multi-class classification [15]
- Avanti-WSI prostate multi-label classification [43]
- Cyto-WSI bone marrow single cell multi-class classification [44]
- Chexpert-CXR Thorax pathology multi-label classification [45]
- SIIM-CXR pneumothorax semantic segmentation [46]

In addition, we included the following auxiliary datasets for the purpose of meta-learning. Unlike the other pretraining tasks, they did not focus on resolving a specific clinical issue:

- ImageNet real world image classification [1]
- RadImageNet radiology multi-class classification [4]
- COCO real world semantic segmentation [47]
- COCO real world object detection [47]

### **Data augmentation**

For 3D tomographic images, we applied standard 3D augmentations, followed by slicing and a set of standard domain specific 2D augmentations. We augmented the orientation of the volume if the maximum edge length was more than two times the shortest edge length as proposed in [48].

For 2D images, we used standard augmentations using the albumentations library [49] (CLAHE, Sharpen, Emboss, RandomBrightnessContrast, RandomGamma, Gaussnoise and HueSaturationValue, ShiftScaleRotate). For X-ray images we added image inversion with a 30% probability, for histological imaging flips and channel shuffle and for MRI images flips and mirroring.

## Task types

### Classification

In the classification task, we handled data where a single input was associated with a single classification label from a set of  $C$  classes. We used the latent representation computed by the encoder and processed it through a fully connected layer to obtain classification scores.

For classification tasks, we employed categorical cross-entropy  $\mathcal{L}_{CCE}$  to compute the loss as implemented in [50]. Typically, the loss magnitude would increase with a larger number of classes  $C$ . To prevent a bias towards tasks with more classes, we added a normalization term  $\log C$  to compute the final loss as

$$\mathcal{L}_{\text{multiclass}}(\hat{y}, y) = \mathcal{L}_{CCE}(\hat{y}, y) \cdot \log C, \quad (1)$$

where  $\hat{y} \in \mathbb{R}^C$  and  $y \in \{0, 1, \dots, C\}$  are the true and predicted labels, respectively.

We did not utilize label smoothing or class probabilities in the classification task.

For multi-label classification tasks, we considered inputs that each had multiple binary classification targets  $y$ . In these cases, we chose the binary cross-entropy loss  $\mathcal{L}_{BCE}$  from [50]. To normalize the loss to 1, we multiplied with a constant factor  $\log_2(\exp(1)) \approx 1.44269$ :

$$\mathcal{L}_{\text{multilabel}}(\hat{y}, y) = \mathcal{L}_{BCE} \cdot 1.44269 \quad (2)$$

### Semantic segmentation task

The U-net architecture consisted of an encoder and a decoder, with the decoder producing dense pixel-level embeddings as output. To generate the final output, skip connections were established between the encoder's feature maps and the decoder's upsampling layers. These skip connections were implemented by concatenating the corresponding feature maps with the decoder's upsampling outputs. For training, we adopted the U-net decoder from [51], which is an implementation of the original U-Net formulation proposed by [52].

The semantic segmentation task aimed to assign a class label to each pixel within an image, with the targets consisting of classes ranging from 1 to  $C$ . For UMedPT we configured its encoder to yield feature maps with strides of 4, 8, 16 and 32.

We employed an equally weighted combination of Dice loss and Focal loss for all segmentation tasks in UMedPT. This strategy was chosen because Dice loss has been shown to perform well for mildly skewed datasets [53], while Focal loss is particularly effective for highly imbalanced datasets [54]. Thus, this combination allowed us to address challenges associated with both balanced and imbalanced datasets, such as the presence of large background regions, without the need for hyperparameter tuning.

## Object detection task

FCOS (Fully Convolutional One-Stage) [33] is an anchor-free object detection method, which makes it an ideal candidate for our multi-task learning approach due to its similarity with our segmentation and classification methods, enabling efficient feature reuse.

Instead of traditional anchor-box based detection, FCOS employed pixel-dense predictions and a box-postprocessing technique. The architecture incorporated a shared encoder and a detection-specific decoder that produced two branches: one for classification and another for bounding box regression. The classification branch managed multi-class classification and centerness per pixel, while the bounding box regression branch predicted rectangle parameters, specifically the distances from each pixel to the edges of the bounding box. Although centerness is not essential to the algorithm, it helps suppressing low-quality bounding boxes. The final score for a box was computed by multiplying the predicted center-ness with the corresponding classification score. To ensure homogeneity in the magnitudes of all multi-task losses and facilitate multi-task learning, we normalized the classification loss by dividing it by the number of classes  $C$ . This resulted in the following combined loss function:  $\mathcal{L}_{\text{objectdetection}} = \mathcal{L}_{\text{classification}} \cdot \frac{1}{C} + \mathcal{L}_{\text{regression}} + \mathcal{L}_{\text{centerness}}$ .

To reconstruct bounding boxes, the network produced a classification score per pixel, a centerness value, and rectangle parameters. Centerness was shared among tasks, fostering efficient multi-task learning, while each detection task employed one convolutional layer for classification and one convolutional layer for regression. Similar to our segmentation task, the forward pass of the detection task generated one feature map for each downsampling step, typically resulting in five feature maps. These multi-level feature maps encapsulated spatial and semantic information at multiple resolutions, enhancing the method's efficacy in object detection and enabled encoding difficult ground truth cases involving overlapping and variably sized boxes.

## Clinical validation

UMedPT was clinically validated using a diverse set of clinically relevant tasks. Our evaluation centered on two main aspects: the model's skill generalizability to new tasks and its proficiency in retrieving previously learned knowledge. These aspects were evaluated using two distinct benchmarks. We developed the downstream training schedule and tuned the hyperparameters using a simple synthetic dataset and ran the clinical evaluation exactly once without further hyperparameter tuning. For this reason, we did not use a validation set in our experiments.

The "in-domain" benchmark tested the model's ability to recall and adapt learned skills to new tasks. The "out-of-domain" benchmark measured the model's ability to adapt its learned skills to tasks distinct from the ones in the pretraining database.

Two distinct usage settings were considered in our evaluation: frozen and fine-tuning. In the frozen scenario, we directly extracted image representations from the shared blocks, thereby showing the usefulness of the learned representations. Subsequently, the fine-tuning stage enabled the training of the shared blocks. The learning rates for the shared blocks in the transformer were set at  $10^{-5}$ , while the task-specific sections of the target tasks were trained at learning rates of  $10^{-4}$ .

To simulate data-scarcity and evaluate sample efficiency, we took multiple samples from the original training set at sizes of 1%, 5%, 10%, 25%, 50%, and 100%. We utilized five splits of the training data to account for random selection effects, and ensured that all data from smaller splits also appear in the corresponding larger splits. Each method was evaluated for exactly the same five random train-test-splits. In consequence, a paired t-test was applied (significance level  $p < 0.05$ ), treating each baseline-UMedPT result on a single train/test split as a pair.

### **In-domain benchmark**

We formulated a benchmark that aimed at examining the recoverability of knowledge encapsulated in UMedPT. We selected knowledge already present in the pretraining database and examined their re-discovery potential by measuring the number of samples needed for re-identification, and compared the outcome with the ImageNet baseline on novel images.

#### ***CRC tissue classification (CRC-WSI):***

The CRC-WSI dataset consisted of Hematoxylin and Eosin (HE) stained images with nine tissue classifications that are largely balanced. The training set comprised 100,000 images extracted from 86 whole slide images, while the test data came from 25 different CRC patients. The label type of the CRC-WSI task was multi-class classification.

#### ***Pneumonia in pediatric cohort (Pneumo-CXR):***

The Pneumo-CXR dataset [16] consisted of pediatric chest X-rays, each labelled as either normal or pneumonia. Consistent with our approach for all datasets, we preserved the original label imbalance when downsizing the training datasets. The training set contained 1,349 normal cases and 3,883 pneumonia cases, while the test set contained 234 normal cases and 390 pneumonia cases. We treated Pneumo-CXR as a multi-class classification task with two classes.

### **Out-of-domain benchmark**

Here, we evaluated the transfer effectiveness of our method across a variety of clinically relevant tasks by establishing an out-of-domain generalization benchmark. In this benchmark each task's domain had to be different from all domains of the pretraining tasks. We were able to increase the certainty of

this claim by including only supervised pretraining tasks. Since the problem setting for each sample in a supervised task is known, this approach reduced the likelihood of pretraining knowledge overlapping with the benchmark.

### ***Tuberculosis diagnosis in CXR (Tuber-CXR):***

The Tuber-CxR dataset [17] consisted of postero-anterior (PA) chest radiographs that we used for multi-class classification. We randomly divided the images into a training set (70% of the data) and a test set (30% of the data) prior to any evaluation. The training set contained 239 tuberculosis samples and 225 normal samples, while the test set contained 51 tuberculosis samples and 101 normal samples. This dataset was used as a multi-class classification task and considered out-of-domain because none of the pretraining datasets had tuberculosis labels.

### ***CNS neoplasia diagnosis in MRI (CNS-MRI):***

The dataset of the CNS-MRI multi-class classification task [18] consisted of 7,023 2D slices derived from MRI scans categorized into four classes: glioma, meningioma, no tumor, and pituitary tumor. The slices originate from T1, T2 and FLAIR sequences and were selected by the authors of the dataset. Prior to any evaluation, we randomly partitioned the images into a training set containing 70% of the data and a test set containing the remaining 30%.

### ***Breast cancer classification in WSI (BC-Bach-WSI):***

The dataset of the BC-Bach-WSI multi-class classification task [21] was used for breast cancer classification in HE-stained whole histological slide images (WSIs). It consisted of four classes: normal, benign tumors, as well as in-situ and invasive carcinomas. The dataset was derived from 30 WSIs and was divided into image patches by the authors of the dataset. Each resulting image was annotated by two expert pathologists. From these images we used 76 normal tissues, 79 benign tumors, 80 in situ carcinomas, and 85 invasive cancers for training. For testing, we used 24 normal, 21 benign, 20 in situ, and 15 invasive images.

### ***Breast cancer classification in microscopic images (BC-BHis-MIC):***

The dataset of the BC-BHis-MIC multi-class classification task focused on the binary classification of microscopic images from HE-stained breast tumors into benign lesions as opposed to malignant tumors [55]. Benign lesions included adenosis, fibroadenoma, phylloides tumor, and tubular adenoma. The malignant tumor class contained 4 subtypes of invasive carcinoma: ductal carcinoma (currently referred to as "unspecific type"), lobular carcinoma, mucinous carcinoma, and papillary carcinoma. The authors of the dataset had achieved a maximum AUC at 200X magnification, which we also adopted for our analysis. The dataset contained 7,909 image patches from 82 patients, with 2,480 benign and 5,429 malignant images. To prepare for evaluation, we randomly

divided the images into a training set (70% of the data) and a test set (30% of the data) prior to any analysis.

### ***Organ segmentation in MRI (OrganSeg-MRI):***

The organ segmentation in MRI dataset OrganSeg-MRI was part of the AMOS22 challenge data [19] and consisted of 60 MRI volumes, split into 40 for training and 20 for testing. Each volume came with annotations for 15 different organs, spleen, right kidney, left kidney, gallbladder, esophagus, liver, stomach, aorta, inferior vena cava, pancreas, right adrenal gland, left adrenal gland, duodenum, bladder, and either the prostate or uterus.

### **Comparison of benchmark results**

We compared our results to the best study results previously reported for the seven target tasks. In this context, we determined the percentage of data that UMedPT required to achieve performance comparable to the external reference result. For each target task, the evaluation criteria from the respective reference papers were used. In 4 of 7 cases, the data set had to be split manually because the creators had not defined the test data. In these cases, manual splitting was performed only once to avoid bias.

### **Application of UMedPT in an external multi-center validation of colorectal tumor diagnosis models**

*Due to an embargo this section will be updated after 01.01.24*

## **Data availability**

The raw data required to make the plots are distributed within the Source Data section. The training and evaluation data were obtained from their original repositories as listed below:

- Amos22 [19] (organ segmentation in CT & MRI): <https://amos22.grand-challenge.org/>
- Conic-WSI [37] (cell detection): <https://conic-challenge.grand-challenge.org/>
- PICAL-MRI [38] (prostate cancer classification) <https://pi-cai.grand-challenge.org/>:
- Panda-WSI [39] (prostate tissue semantic segmentation & classification): <https://www.kaggle.com/c/prostate-cancer-grade-assessment>
- VinBigData-CXR [40] (Thorax pathology pathology detection): <https://www.kaggle.com/competitions/vinbigdata-chest-xray-abnormalities-detection>
- Crag-WSI [41] (Colorectal tissue semantic segmentation): [https://github.com/XiaoyuZHK/CRAG-Dataset\\_Aug\\_ToCOCO](https://github.com/XiaoyuZHK/CRAG-Dataset_Aug_ToCOCO)
- Brats2020-MRI [42] (brain semantic segmentation): <https://www.kaggle.com/datasets/awsaf49/brats20-dataset-training-validation>

- Avanti-WSI [43] (prostate multi-label classification): <https://doi.org/10.7910/DVN/OCYCMP>
- Cyto-WSI [44] (bone marrow single cell multi-class classification): <https://wiki.cancerimagingarchive.net/pages/viewpage.action?pageId=101941770>
- Chexpert-CXR [45] (Thorax pathology multi-label classification): <https://stanfordaimi.azurewebsites.net/datasets/8cbd9ed4-2eb9-4565-affc-111cf4f7ebe2> & <https://github.com/rajpurkarlab/cheXpert-test-set-labels>
- SIIM-CXR [46] (pneumothorax semantic segmentation): <https://www.kaggle.com/competitions/siim-acr-pneumothorax-segmentation/data>
- ImageNet [1] (real world image classification): <https://www.image-net.org/download.php>
- RadImageNet [4] (radiology multi-class classification): request access at <https://www.radimagenet.com/copy-of-home-1>
- COCO [47] (real world semantic segmentation & object detection): <https://cocodataset.org/#download>
- CRC-WSI [15] (colorectal cancer tissue classification): <https://zenodo.org/record/1214456>
- Pneumo-CXR [16] (pneumonia in pediatric cohort): <https://data.mendeley.com/datasets/rscbjbr9sj/3>
- Tuber-CXR [17] (tuberculosis diagnosis in CXR): <https://www.kaggle.com/datasets/raddar/tuberculosis-chest-xrays-shenzhen>
- CNS-MRI [18] (CNS neoplasia diagnosis in MRI): <https://www.kaggle.com/datasets/masoudnickparvar/brain-tumor-mri-dataset>
- BC-Bach-WSI [21] (breast cancer classification in WSI): <https://iciar2018-challenge.grand-challenge.org/>
- BC-BHis-MIC [55] (breast cancer classification in microscopic images): <https://web.inf.ufpr.br/vri/databases/breast-cancer-histopathological-database-breakhis/>

## Code availability

The code for reproducing our results is available at <https://zenodo.org/will/be/added/in/final/version>. This archive contains the code for all experiments, including the corresponding archived version of the training framework.

If you intend to use UMedPT or its training framework, we recommend that you use the latest version from the respective public projects hosted on Github. The general training strategy is maintained as a Python package at: <https://github.com/FraunhoferMEVIS/will/be/added/in/final/version>. The latest version of UMedPT can be found at: <https://github.com/FraunhoferMEVIS/will/be/added/in/final/version>.

## References

- [1] Deng, J. *et al.* Imagenet: A large-scale hierarchical image database. *2009 IEEE Conference on Computer Vision and Pattern Recognition* 248–255

- (2009). <https://doi.org/10.1109/CVPR.2009.5206848> .
- [2] Kim, H. E. *et al.* Transfer learning for medical image classification: a literature review. *BMC Medical Imaging* **22** (1), 69 (2022). <https://doi.org/10.1186/s12880-022-00793-7> .
- [3] Kather, J. N. *et al.* Deep learning can predict microsatellite instability directly from histology in gastrointestinal cancer. *Nature medicine* **25** (7), 1054–1056 (2019). <https://doi.org/10.1038/s41591-019-0462-y> .
- [4] Mei, X. *et al.* Radimagenet: an open radiologic deep learning research dataset for effective transfer learning. *Radiology: Artificial Intelligence* **4** (5), e210315 (2022). <https://doi.org/10.1148/ryai.210315> .
- [5] Raghu, M., Zhang, C., Kleinberg, J. M. & Bengio, S. Transfusion: Understanding transfer learning with applications to medical imaging. *CoRR* **abs/1902.07208** (2019). <https://arxiv.org/abs/1902.07208> .
- [6] Wang, X. *et al.* Chestx-ray8: Hospital-scale chest x-ray database and benchmarks on weakly-supervised classification and localization of common thorax diseases. *CoRR* **abs/1705.02315** (2017). <https://arxiv.org/abs/1705.02315> .
- [7] Moor, M. *et al.* Foundation models for generalist medical artificial intelligence. *Nature* **616** (7956), 259–265 (2023). URL <https://doi.org/10.1038/s41586-023-05881-4> .
- [8] Willemink, M. J., Roth, H. R. & Sandfort, V. Toward foundational deep learning models for medical imaging in the new era of transformer networks. *Radiology: Artificial Intelligence* **4** (6), e210284 (2022). <https://doi.org/10.1148/ryai.210284> .
- [9] Litjens, G. *et al.* A survey on deep learning in medical image analysis. *Medical Image Analysis* **42**, 60–88 (2017). <https://doi.org/10.1016/j.media.2017.07.005> .
- [10] Zhou, H.-Y. *et al.* Generalized radiograph representation learning via cross-supervision between images and free-text radiology reports. *Nature Machine Intelligence* **4** (1), 32–40 (2022). <https://doi.org/10.1038/s42256-021-00425-9> .
- [11] Zhang, Y. & Yang, Q. A survey on multi-task learning. *IEEE Transactions on Knowledge and Data Engineering* **34** (12), 5586–5609 (2022). <https://doi.org/10.1109/TKDE.2021.3070203> .
- [12] Mormont, R., Geurts, P. & Marée, R. Multi-task pre-training of deep neural networks for digital pathology. *IEEE Journal of Biomedical and Health*

- Informatics* **25** (2), 412–421 (2021). <https://doi.org/10.1109/JBHI.2020.2992878> .
- [13] Chen, J. *et al.* Transunet: Transformers make strong encoders for medical image segmentation (2021). URL <https://arxiv.org/abs/2102.04306>.
- [14] Graham, S. *et al.* One model is all you need: Multi-task learning enables simultaneous histology image segmentation and classification (2022). URL <https://arxiv.org/abs/2203.00077>.
- [15] Kather, J. N. *et al.* Predicting survival from colorectal cancer histology slides using deep learning: A retrospective multicenter study. *PLoS medicine* **16** (1), e1002730 (2019). <https://doi.org/10.1371/journal.pmed.1002730> .
- [16] Kermany, D. S. *et al.* Identifying medical diagnoses and treatable diseases by image-based deep learning. *Cell* **172** (5), 1122–1131.e9 (2018). URL <https://www.sciencedirect.com/science/article/pii/S0092867418301545>. <https://doi.org/10.1016/j.cell.2018.02.010> .
- [17] Jaeger, S. *et al.* Two public chest x-ray datasets for computer-aided screening of pulmonary diseases. *Quantitative imaging in medicine and surgery* **4** (6), 475 (2014). <https://doi.org/10.3978/j.issn.2223-4292.2014.11.20> .
- [18] Brain tumor mri dataset. Available at: <https://www.kaggle.com/datasets/masoudnickparvar/brain-tumor-mri-dataset> (2020). Accessed: 2023-01-14.
- [19] Ji, Y. *et al.* Amos: A large-scale abdominal multi-organ benchmark for versatile medical image segmentation (2022). <https://arxiv.org/abs/2206.08023> [eess.IV].
- [20] Jaeger, S. *et al.* Automatic tuberculosis screening using chest radiographs. *IEEE transactions on medical imaging* **33** (2), 233–245 (2013). <https://doi.org/10.1109/TMI.2013.2284099> .
- [21] Aresta, G. *et al.* Bach: Grand challenge on breast cancer histology images. *Medical Image Analysis* **56**, 122–139 (2019). URL <https://www.sciencedirect.com/science/article/pii/S1361841518307941>. <https://doi.org/10.1016/j.media.2019.05.010> .
- [22] Chhipa, P. C. *et al.* Magnification prior: A self-supervised method for learning representations on breast cancer histopathological images (2022). <https://arxiv.org/abs/2203.07707> .

- [23] Singhal, K. *et al.* Large language models encode clinical knowledge. *Nature* 1–9 (2023). <https://doi.org/10.1038/s41586-023-06291-2> .
- [24] Radford, A. *et al.* Learning transferable visual models from natural language supervision 8748–8763 (2021). <https://arxiv.org/abs/2103.00020> .
- [25] Kirillov, A. *et al.* Segment anything (2023). <https://arxiv.org/abs/2304.02643> [cs.CV].
- [26] Oliver, A., Odena, A., Raffel, C. A., Cubuk, E. D. & Goodfellow, I. Realistic evaluation of deep semi-supervised learning algorithms. *Advances in neural information processing systems* **31** (2018). <https://arxiv.org/abs/1804.09170> .
- [27] Castro, D. C., Walker, I. & Glocker, B. Causality matters in medical imaging. *Nature Communications* **11** (1), 3673 (2020). <https://doi.org/10.1038/s41467-020-17478-w> .
- [28] Yadav, P., Menon, N., Ravi, V. & Vishvanathan, S. Lung-gans: Unsupervised representation learning for lung disease classification using chest ct and x-ray images. *IEEE Transactions on Engineering Management* **70** (8), 2774–2786 (2023). <https://doi.org/10.1109/TEM.2021.3103334> .
- [29] Arun Prakash, J., Asswin, C., Ravi, V., Sowmya, V. & Soman, K. Pediatric pneumonia diagnosis using stacked ensemble learning on multi-model deep cnn architectures. *Multimedia Tools and Applications* **82** (14), 21311–21351 (2023). <https://doi.org/10.1007/s11042-022-13844-6> .
- [30] Sarma, K. V. *et al.* Federated learning improves site performance in multicenter deep learning without data sharing. *Journal of the American Medical Informatics Association* **28** (6), 1259–1264 (2021). URL <https://doi.org/10.1093/jamia/ocaa341>, <https://doi.org/10.1093/jamia/ocaa341>, <https://arxiv.org/abs/https://academic.oup.com/jamia/article-pdf/28/6/1259/38615457/ocaa341.pdf> .
- [31] Loshchilov, I. & Hutter, F. Decoupled weight decay regularization. *International Conference on Learning Representations* (2019). URL <https://openreview.net/forum?id=Bkg6RiCqY7>.
- [32] Liu, Z. *et al.* Swin transformer: Hierarchical vision transformer using shifted windows (2021). URL <https://doi.ieeecomputersociety.org/10.1109/ICCV48922.2021.00986>.
- [33] Tian, Z., Shen, C., Chen, H. & He, T. Fcos: A simple and strong anchor-free object detector. *IEEE Transactions on Pattern Analysis and Machine Intelligence* **44** (4), 1922–1933 (2022). <https://doi.org/10.1109/TPAMI>.

2020.3032166 .

- [34] Lin, T.-Y. *et al.* Feature pyramid networks for object detection (2017). <https://arxiv.org/abs/1612.03144> [cs.CV].
- [35] Ioffe, S. & Szegedy, C. Batch normalization: Accelerating deep network training by reducing internal covariate shift. *CoRR* **abs/1502.03167** (2015). <https://doi.org/10.48550/arXiv.1502.03167>, <https://arxiv.org/abs/1502.03167> .
- [36] Ba, J. L., Kiros, J. R. & Hinton, G. E. Layer normalization (2016). <https://arxiv.org/abs/1607.06450> [stat.ML].
- [37] Graham, S. *et al.* Lizard: A large-scale dataset for colonic nuclear instance segmentation and classification (2021). URL <https://doi.ieeecomputersociety.org/10.1109/ICCVW54120.2021.00082>.
- [38] Saha, A. *et al.* Artificial Intelligence and Radiologists at Prostate Cancer Detection in MRI: The PI-CAI Challenge (Study Protocol) (2022). <https://doi.org/10.5281/zenodo.6667655> .
- [39] Bulten, W. *et al.* Artificial intelligence for diagnosis and gleason grading of prostate cancer: the panda challenge. *Nature medicine* **28** (1), 154–163 (2022). <https://doi.org/10.1038/s41591-021-01620-2> .
- [40] DungNB *et al.* Vinbigdata chest x-ray abnormalities detection (2020). URL <https://kaggle.com/competitions/vinbigdata-chest-xray-abnormalities-detection>.
- [41] Graham, S., Chen, H., Dou, Q., Heng, P. & Rajpoot, N. M. Mild-net: Minimal information loss dilated network for gland instance segmentation in colon histology images. *CoRR* **abs/1806.01963** (2018). <https://arxiv.org/abs/1806.01963> .
- [42] Menze, B. H. *et al.* The multimodal brain tumor image segmentation benchmark (brats). *IEEE transactions on medical imaging* **34** (10), 1993–2024 (2014). <https://doi.org/10.1109/TMI.2014.2377694> .
- [43] Arvaniti, E. *et al.* Automated gleason grading of prostate cancer tissue microarrays via deep learning. *Scientific reports* **8** (1), 12054 (2018). <https://doi.org/10.1038/s41598-018-30535-1> .
- [44] Matek, C., Krappe, S., Münzenmayer, C., Haferlach, T. & Marr, C. Highly accurate differentiation of bone marrow cell morphologies using deep neural networks on a large image data set. *Blood, The Journal of the American Society of Hematology* **138** (20), 1917–1927 (2021). <https://doi.org/10.1182/blood.2020010568> .

- [45] Irvin, J. *et al.* Chexpert: A large chest radiograph dataset with uncertainty labels and expert comparison (2019). <https://arxiv.org/abs/1901.07031> [cs.CV].
- [46] Langer, S. G. & Shih, G. Siim-acr pneumothorax segmentation (2020). URL <https://www.kaggle.com/competitions/siim-acr-pneumothorax-segmentation/data>. Retrieved 27-09-2022.
- [47] Lin, T.-Y. *et al.* Fleet, D., Pajdla, T., Schiele, B. & Tuytelaars, T. (eds) *Microsoft coco: Common objects in context*. (eds Fleet, D., Pajdla, T., Schiele, B. & Tuytelaars, T.) *Computer Vision – ECCV 2014*, 740–755 (Springer International Publishing, Cham, 2014). [https://doi.org/10.1007/978-3-319-10602-1\\_48](https://doi.org/10.1007/978-3-319-10602-1_48).
- [48] Isensee, F., Jaeger, P. F., Kohl, S. A. A., Petersen, J. & Maier-Hein, K. H. nnu-net: a self-configuring method for deep learning-based biomedical image segmentation. *Nature Methods* **18** (2), 203–211 (2021). <https://doi.org/10.1038/s41592-020-01008-z> .
- [49] Buslaev, A., Parinov, A., Khvedchenya, E., Iglovikov, V. I. & Kalinin, A. A. Albumentations: fast and flexible image augmentations. *ArXiv e-prints* (2018). <https://arxiv.org/abs/1809.06839> .
- [50] Paszke, A. *et al.* Pytorch: An imperative style, high-performance deep learning library (2019). <https://arxiv.org/abs/1912.01703> [cs.LG].
- [51] Iakubovskii, P. Segmentation models pytorch. [https://github.com/qubvel/segmentation\\_models.pytorch](https://github.com/qubvel/segmentation_models.pytorch) (2019).
- [52] Ronneberger, O., Fischer, P. & Brox, T. Navab, N., Hornegger, J., Wells, W. M. & Frangi, A. F. (eds) *U-net: Convolutional networks for biomedical image segmentation*. (eds Navab, N., Hornegger, J., Wells, W. M. & Frangi, A. F.) *Medical Image Computing and Computer-Assisted Intervention – MICCAI 2015*, 234–241 (Springer International Publishing, Cham, 2015). [https://doi.org/10.1007/978-3-319-24574-4\\_28](https://doi.org/10.1007/978-3-319-24574-4_28).
- [53] Jadon, S. A survey of loss functions for semantic segmentation. *2020 IEEE Conference on Computational Intelligence in Bioinformatics and Computational Biology (CIBCB)*, 1-7 (2020). <https://doi.org/10.1109/CIBCB48159.2020.9277638>.
- [54] Lin, T.-Y., Goyal, P., Girshick, R., He, K. & Dollár, P. Focal loss for dense object detection. *IEEE Transactions on Pattern Analysis and Machine Intelligence* **42** (2), 318–327 (2020). <https://doi.org/10.1109/TPAMI.2018.2858826> .

- [55] Spanhol, F. A., Oliveira, L. S., Petitjean, C. & Heutte, L. A dataset for breast cancer histopathological image classification. *IEEE Transactions on Biomedical Engineering* **63** (7), 1455–1462 (2016). <https://doi.org/10.1109/TBME.2015.2496264> .

## Acknowledgements

This research was partly funded by the German ministry of education and research (BMBF) through the project SynDICAD (01IS21067C).

## Author information

RS and TN built pretraining and benchmark databases and implemented software. RS conducted the experiments, analyzed the results, and wrote the manuscript, with feedback from all authors. TN generated the plots and diagrams, and analyzed the results. AL, DM, HH, FF, VS revised the manuscript. FF: pathology advisor. JL: coordinated the study. FK: coordinated the study, radiology advisor.

## Supplement

**Extended Data Table 1 In-domain benchmark results.** The left pair of columns shows results with a frozen encoder, while the right pair shows results with fine-tuning (F1-scores reported in percentage). P-values, calculated independently for each dataset size, were always compared against the pretrained ImageNet model. UMedPT-fixed was an ablation study where patch sizes remained constant, and UMedPT-A was another ablation where layernorms had trainable parameters.

Size	Model	frozen		finetune	
		PPneumo-CXR	CRC-WSI	PPneumo-CXR	CRC-WSI
1%	ImageNet	61.68±12.55%	80.81±0.54%	85.54±2.32%	91.84±1.70%
	UMedPT fixed	89.06±1.39% p=4.54e-03	97.03±0.07% p=3.13e-07	91.52±1.97% p=2.19e-02	96.53±0.61% p=2.58e-03
	UMedPT affine	88.51±1.71% p=5.54e-03	97.17±0.08% p=2.96e-07	91.71±1.97% p=1.74e-02	96.98±0.76% p=7.02e-04
	UMedPT	91.97±1.57% p=3.09e-03	95.37±0.13% p=8.26e-07	92.81±0.82% p=2.18e-03	95.97±0.64% p=2.32e-03
5%	ImageNet	78.07±1.27%	84.91±0.35%	84.80±1.99%	94.64±0.82%
	UMedPT fixed	89.49±1.29% p=8.35e-05	96.96±0.11% p=2.27e-07	91.34±1.84% p=1.79e-03	96.57±0.34% p=3.98e-03
	UMedPT affine	88.24±1.44% p=9.74e-05	96.96±0.15% p=1.82e-08	91.04±2.01% p=5.33e-04	96.78±0.30% p=7.52e-03
	UMedPT	93.46±0.65% p=1.14e-06	95.45±0.14% p=6.89e-07	92.02±2.03% p=6.77e-04	95.68±0.70% p=7.90e-02
10%	ImageNet	79.05±1.54%	86.13±0.35%	85.06±6.84%	95.44±0.56%
	UMedPT fixed	87.63±2.51% p=1.02e-04	97.04±0.17% p=2.65e-07	90.05±3.06% p=8.43e-02	96.45±0.32% p=5.16e-03
	UMedPT affine	87.50±2.86% p=2.06e-04	96.91±0.22% p=1.99e-07	89.79±2.62% p=8.19e-02	95.83±0.46% p=1.25e-01
	UMedPT	91.95±1.52% p=2.16e-05	95.20±0.40% p=7.47e-06	91.08±2.75% p=3.12e-02	95.55±0.61% p=3.93e-01
50%	ImageNet	81.53±0.57%	87.61±0.12%	88.81±2.85%	95.69±0.68%
	UMedPT fixed	89.56±0.76% p=3.93e-05	96.83±0.13% p=1.72e-08	90.50±3.02% p=1.91e-02	95.70±0.68% p=4.90e-01
	UMedPT affine	89.65±0.64% p=2.60e-05	96.70±0.12% p=4.67e-11	92.16±1.04% p=3.42e-02	95.78±0.76% p=4.37e-01
	UMedPT	90.52±0.35% p=2.26e-07	95.59±0.13% p=4.43e-08	90.58±1.94% p=2.22e-01	95.01±0.69% p=8.68e-01
100%	ImageNet	82.18±0.94%	87.68±0.07%	90.34±1.77%	95.16±0.59%
	UMedPT fixed	90.14±0.66% p=8.95e-06	96.82±0.08% p=4.69e-10	90.17±0.44% p=5.83e-01	94.93±0.61% p=6.80e-01
	UMedPT affine	90.01±0.48% p=2.18e-05	96.59±0.02% p=4.60e-10	90.61±2.28% p=4.42e-01	95.60±0.33% p=9.77e-02
	UMedPT	89.36±0.31% p=3.40e-05	95.57±0.06% p=1.43e-09	90.73±1.60% p=3.65e-01	94.98±1.09% p=5.94e-01

**Extended Data Table 2 Out-of-domain benchmark with frozen encoder.**

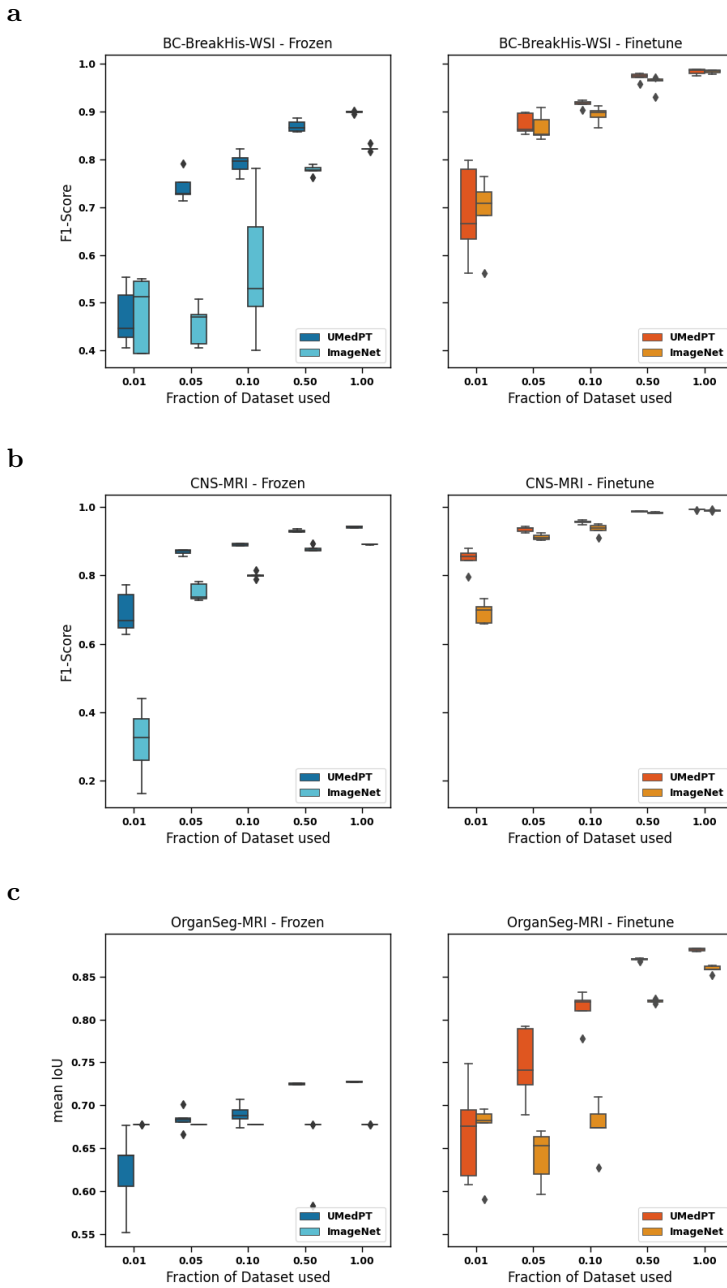
OrganSeg-MRI was evaluated using the mean Intersection over Union (mIoU) metric; all other tasks were analysed using F1-score (reported in percentage). P-values, calculated independently for each dataset size, were always compared against the pretrained ImageNet model. UMedPT-fixed was an ablation study where patch sizes remained constant, and UMedPT-A was another ablation where layernorms had trainable parameters.

Size	Model	Tuber-CXR	OrganSeg-MRI	CNS-MRI	BC-BHis-MIC	BC-BACH-WSI
1%	ImageNet	37.88±5.86%	67.78±0.00%	31.49±9.61%	47.94±7.05%	32.98±3.58%
	UMedPT fixed	55.70±14.94% p=2.27e-02	63.33±4.37% p=9.44e-01	31.69±9.12% p=4.73e-01	47.79±7.68% p=5.20e-01	26.99±5.51% p=8.87e-01
	UMedPT affine	55.66±13.27% p=1.75e-02	64.52±2.29% p=9.77e-01	37.18±7.00% p=7.53e-02	55.14±11.11% p=6.43e-02	33.19±8.92% p=4.82e-01
	UMedPT	51.63±16.87% p=4.38e-02	62.36±4.22% p=9.69e-01	69.18±5.68% p=7.19e-05	46.94±5.56% p=6.24e-01	34.64±10.00% p=3.94e-01
5%	ImageNet	46.87±14.45%	67.78±0.00%	75.14±2.31%	45.41±3.91%	20.19±10.31%
	UMedPT fixed	67.62±3.28% p=1.11e-02	66.93±0.72% p=9.62e-01	80.21±2.85% p=1.06e-03	55.47±4.68% p=4.58e-03	26.26±9.31% p=1.64e-01
	UMedPT affine	68.30±6.40% p=2.77e-02	67.37±0.15% p=9.97e-01	78.15±3.69% p=7.35e-03	61.37±9.69% p=4.71e-03	33.10±13.31% p=6.64e-02
	UMedPT	76.67±16.65% p=5.88e-03	68.30±1.13% p=2.06e-01	86.80±0.76% p=1.35e-04	74.23±2.77% p=6.52e-06	29.78±12.12% p=8.18e-02
10%	ImageNet	50.42±11.04%	67.78±0.00%	80.03±0.84%	57.23±13.31%	39.90±8.90%
	UMedPT fixed	76.18±2.57% p=1.97e-03	67.23±0.61% p=9.27e-01	84.82±0.74% p=8.57e-06	61.34±11.47% p=2.13e-01	47.70±15.34% p=7.10e-02
	UMedPT affine	76.25±4.73% p=1.87e-03	67.57±0.24% p=9.22e-01	84.22±1.04% p=7.93e-05	68.03±8.56% p=1.86e-02	51.29±14.69% p=5.00e-02
	UMedPT	86.42±2.12% p=9.65e-04	68.97±1.09% p=4.73e-02	88.95±0.33% p=5.82e-06	79.17±2.12% p=9.91e-03	56.83±14.76% p=4.62e-03
50%	ImageNet	70.42±4.14%	65.88±3.81%	87.83±0.81%	77.76±0.93%	61.24±2.71%
	UMedPT fixed	85.03±1.10% p=1.56e-03	68.11±0.13% p=1.58e-01	91.65±0.28% p=5.36e-04	84.12±0.26% p=2.45e-05	70.63±6.97% p=2.59e-02
	UMedPT affine	84.18±1.32% p=1.78e-03	67.84±0.01% p=1.80e-01	90.68±0.38% p=3.27e-03	85.18±1.42% p=1.37e-03	75.92±3.07% p=2.17e-04
	UMedPT	90.50±0.91% p=3.88e-04	72.48±0.08% p=1.34e-02	92.95±0.33% p=1.53e-04	86.94±1.14% p=4.44e-05	77.97±0.96% p=1.84e-04
100%	ImageNet	67.99±1.11%	67.78±0.00%	89.05±0.11%	82.30±0.58%	72.90±1.49%
	UMedPT fixed	86.89±0.93% p=6.22e-07	68.49±0.06% p=9.02e-06	93.33±0.11% p=3.37e-07	87.15±0.31% p=1.32e-04	80.98±1.28% p=1.09e-03
	UMedPT affine	86.01±0.25% p=1.76e-06	67.87±0.02% p=3.23e-04	92.82±0.20% p=1.19e-06	87.12±0.22% p=4.94e-05	85.84±1.24% p=1.87e-04
	UMedPT	93.50±0.20% p=1.12e-06	72.71±0.03% p=2.21e-10	94.14±0.17% p=1.60e-06	89.87±0.22% p=1.11e-05	81.17±0.43% p=2.39e-04

**Extended Data Table 3 Out-of-domain benchmark with fine-tuned encoder.**

OrganSeg-MRI was evaluated using the mean Intersection over Union (mIoU) metric; all other tasks were analysed using F1-score (reported in percentage). P-values, calculated independently for each dataset size, were always compared against the baseline. ImageNet served as the baseline, with UMedPT representing our model. UMedPT-fixed was an ablation study where patch sizes remained constant, and UMedPT-A was another ablation where layernorms had trainable parameters.

Size	Model	Tuber-CXR	OrganSeg-MRI	CNS-MRI	BC-BHis-MIC	BC-BACH-WSI
1%	ImageNet	58.21±9.50%	66.74±3.90%	69.24±2.81%	68.96±6.90%	36.44±5.12%
	UMedPT fixed	62.70±8.92% p=2.98e-01	63.57±1.01% p=9.32e-01	79.46±1.60% p=3.81e-03	70.87±7.19% p=1.29e-01	38.07±7.64% p=3.29e-01
	UMedPT affine	61.47±11.45% p=3.53e-01	63.31±3.58% p=9.97e-01	75.81±6.93% p=2.08e-02	69.72±6.94% p=3.71e-01	34.81±5.74% p=6.75e-01
	UMedPT	69.54±12.54% p=1.11e-01	66.87±5.17% p=4.79e-01	84.77±2.83% p=4.98e-04	68.79±8.92% p=5.29e-01	41.19±6.57% p=1.34e-01
5%	ImageNet	77.05±3.36%	64.05±2.82%	91.21±0.78%	86.77±2.49%	47.62±7.25%
	UMedPT fixed	83.44±1.85% p=9.78e-03	69.43±3.33% p=4.15e-02	93.57±0.36% p=8.46e-04	88.45±1.63% p=1.22e-02	43.02±6.84% p=9.43e-01
	UMedPT affine	82.44±2.88% p=2.55e-02	69.63±3.80% p=3.74e-02	93.01±0.80% p=7.60e-04	86.39±1.30% p=6.79e-01	42.42±8.40% p=9.44e-01
	UMedPT	92.51±2.36% p=2.80e-04	74.70±3.92% p=2.35e-03	93.50±0.74% p=6.54e-03	87.41±1.96% p=1.27e-01	47.61±12.52% p=5.01e-01
10%	ImageNet	81.17±2.49%	67.49±2.72%	93.53±1.43%	89.29±1.55%	59.84±8.95%
	UMedPT fixed	89.64±0.98% p=1.38e-03	76.42±2.68% p=7.69e-04	95.27±0.66% p=1.12e-02	91.86±0.53% p=1.07e-02	66.42±8.97% p=6.17e-03
	UMedPT affine	88.34±2.59% p=9.94e-03	76.28±2.26% p=1.17e-03	95.24±0.65% p=7.05e-03	91.15±0.57% p=6.92e-02	64.51±9.56% p=6.65e-03
	UMedPT	96.25±1.75% p=5.86e-04	81.25±1.86% p=5.75e-06	95.62±0.47% p=7.18e-03	91.60±0.72% p=3.11e-02	66.54±11.62% p=7.55e-03
50%	ImageNet	88.80±2.20%	82.16±0.20%	98.33±0.19%	95.97±1.44%	83.55±5.42%
	UMedPT fixed	93.01±0.66% p=3.84e-03	86.51±0.16% p=1.75e-06	98.30±0.16% p=5.78e-01	97.21±0.49% p=3.57e-02	89.58±3.20% p=2.23e-02
	UMedPT affine	92.61±0.24% p=1.20e-02	86.34±0.08% p=2.05e-06	98.24±0.15% p=6.93e-01	96.65±0.85% p=5.07e-02	87.87±3.09% p=9.95e-02
	UMedPT	95.44±0.72% p=7.40e-04	87.02±0.13% p=1.58e-06	98.63±0.11% p=2.66e-02	97.20±0.80% p=1.43e-02	88.81±2.79% p=5.68e-02
100%	ImageNet	90.13±4.98%	85.86±0.39%	98.98±0.13%	98.39±0.35%	92.99±2.24%
	UMedPT fixed	94.13±0.82% p=9.53e-02	87.27±0.25% p=2.60e-03	99.27±0.06% p=1.25e-02	98.83±0.19% p=5.34e-02	95.54±1.33% p=6.15e-02
	UMedPT affine	93.12±0.52% p=1.48e-01	87.37±0.36% p=2.70e-04	99.15±0.20% p=6.26e-02	98.23±0.45% p=6.47e-01	94.54±1.61% p=2.09e-01
	UMedPT	93.92±0.46% p=1.11e-01	88.14±0.14% p=1.05e-04	99.27±0.15% p=1.65e-02	98.38±0.60% p=5.07e-01	92.67±2.10% p=5.64e-01



**Extended Data Fig. 1 Results of remaining out-of-distribution tasks. a BC-BHis-MIC b CNS-MRI. c OrganSeg-MRI.**

## S1 State of the art for the tasks

Each item in the list corresponds to one reference result in Table 1.

- **CRC-WSI:** Over 94% accuracy in the nine-class classification problem was achieved with ImageNet transfer learning [15].
- **Pneumo-CXR:** The dataset creators reported a diagnostic accuracy of 92.8%, a sensitivity of 93.2%, and a specificity of 90.1% [16].
- **Tuber-CXR:** Radiologists achieved an accuracy of 82% [20]. Specialized representation learning for CXR achieved an AUC of 98.0%, with their corresponding ImageNet baseline reaching an AUC of 94.5% [10].
- **CNS-MRI:** Classifiers with different data splits from the Kaggle community achieved over 96% accuracy.
- **BC-Bach-WSI:** An accuracy of 87% was achieved using external validation on a challenge server [21].
- **BC-BHis-MIC:** The dataset creators reported an accuracy between 80% and 85% [55]. The highest reported F1-score was 88% [22].